

# Shift current in 2D Janus Transition-Metal Dichalcogenides: the role of excitons

Yuncheng Mao,<sup>1</sup> Ju Zhou,<sup>2,3</sup> Myrta Grüning,<sup>2,4</sup> and Claudio Attaccalite<sup>1,4</sup>

<sup>1</sup>*CNRS/Aix-Marseille Université, Centre Interdisciplinaire de Nanoscience de Marseille UMR 7325 Campus de Luminy, 13288 Marseille Cedex 9, France*

<sup>2</sup>*School of Mathematics and Physics, Queen's University Belfast, Belfast BT7 1NN, Northern Ireland, UK*

<sup>3</sup>*School of Physical Science and Technology and Jiangsu Key Laboratory of Frontier Material Physics and Devices, Soochow University, Suzhou 215006, People's Republic of China*

<sup>4</sup>*European Theoretical Spectroscopy Facilities (ETSF)*

We study the shift current in two two-dimensional (2D) Janus transition metal dichalcogenides: molybdenum diselenide (MoSSe) and tungsten diselenide (WSSe). The shift current is evaluated using a real-time approach, in which the coupling with an external field is described in terms of a dynamical Berry phase. This approach incorporates electron-hole interactions and quasiparticle band structure renormalization through an effective Hamiltonian derived from many-body perturbation theory. We find that the shift current is strongly enhanced in correspondence of C excitons. An analysis in terms of the electron-hole pairs reveals that electron and hole are localized on different atoms, and thus following an optical excitation, the center of the electron charge is shifted thus giving rise to a significant photocurrent. These results highlight the role played by excitons in the shift-current response of Janus TMDs and demonstrate that these materials are promising building blocks for future photovoltaic devices.

## I. INTRODUCTION

The shift current(SC) is a bulk photovoltaic effect that originates from the nonlinear interaction between light and a noncentrosymmetric crystal when illuminated by a continuous wave. As a second-order nonlinear phenomenon, SC has received significant attention in recent years.<sup>1</sup> It involves the creation of a direct current (DC) within non-centrosymmetric materials when these are illuminated by light, demonstrating their intrinsic potential for application in solar cells. Although SC is a promising mechanism for generating photocurrent without the need for p-n junctions, the short-circuit current—which is closely linked to the power efficiency of a solar cell—is typically low. Therefore, it is crucial to understand the underlying physics of this phenomenon and to identify materials with high SC conductivity.

In a recent work, Cook et al.<sup>1</sup> put forward the designing principles for optimizing the SC. They found that low dimensional systems can display a very strong SC due to a strong density of states due Van Hove singularities. Besides the density of states, in low-dimensional materials, due to the confinement of electrons and the poor screening of electron-electron interaction, the formation of bound states, the excitons, occurs upon the excitation of the material, which further enhances the SC.<sup>2-6</sup> The need for a computational approach including all relevant many-body effects and specifically excitonic effects to predict the SC in materials is testified by the large disagreement between theory and experiments. On the one hand, so far most calculations are carried out at the independent particle level. On the other hand, in experiments there are extrinsic factors, difficult to control and quantify, that may modify the SC. For example in WS<sub>2</sub> nanotubes, a strong SC response was reported deviating significantly from the theoretical prediction.<sup>7</sup> It has been argued that this discrepancy is due either to tube-tube

interactions or the different cross section during the evaluation of SC.<sup>8,9</sup> Yet, the SC in these materials has been calculated neglecting excitonic effects that can, in principle, strongly enhance optical response, and thus the SC, in low-dimensional systems.

In this work, we present a real-time approach for predicting the SC conductivity from first-principles in which the coupling between electrons and light is described in terms of a dynamical Berry phase. The Hamiltonian describing the system is derived from the many-body perturbation theory, which allows us to include correlation effects in both the electronic band structure (see, for example, Aryasetiawan et al.<sup>10</sup>) and the response functions (see, for example, Strinati<sup>11</sup>). We have already applied this approach to predict other nonlinear optical effects, such as second harmonic generation, two-photon absorption, and sum-frequency generation.<sup>12-14</sup> In those cases, we extracted nonlinear susceptibilities from the time-dependent polarization density. Here, we extend the approach to extract nonlinear conductivities from the polarization current.

As an application, we calculate the SC conductivity of two Janus transition metal dichalcogenides (TMDs): MoSSe and WSSe, among the recently synthesized Janus 2D TMDs.<sup>15-17</sup> These materials have attracted a lot of attention from the scientific community due to their peculiar properties. Janus monolayers are a new type of 2D material that breaks out-of-plane symmetry and has a large built-in electric field. Janus 2D TMDs exhibit several interesting properties, such as a strong piezoelectric response, long exciton lifetime and enhanced interlayer coupling due to their intrinsic electric field.<sup>18</sup> Their internal electric field renders Janus material ideal for photocatalysis<sup>19</sup>, and photovoltaic applications<sup>20</sup>. Their stacking-dependent dipole moment can be used to tune their intrinsic properties.<sup>18</sup> Similarly to other nonlinear optical effects, geometrical symmetries play an important

role in determining the SC. With respect to standard TMDs, Janus TMDs lack the  $z \rightarrow -z$ , symmetry and have an out-of-plane dipole allowing for a SC along the  $z$ -direction<sup>21,22</sup>. Furthermore, swapping S with Se atoms switches the chirality of these structures and heterostructures can be designed to enhance the photocurrent.<sup>21</sup>. Regarding the in-plane symmetries (xy-plane), though there are non zero elements of the second-order conductivity tensor, no net SC results for unpolarized light—such as sunlight. It has been shown, that a significant SC can be obtained by breaking the  $C_{3v}$  symmetry either by strain, interaction with a substrate<sup>22,23</sup>, or by forming nanotubes.<sup>24</sup>

In this work, we consider monolayer MoSSe and WSSE with light polarized along the  $y$ -direction and obtain the non zero component of the second-order conductivity tensor  $\sigma_{y;yy}^{(2)}$ .<sup>25</sup> At difference with previous works,<sup>22</sup> we include the effect of electron-hole interactions. Section II presents the theoretical approach and computation details. Section III A shows the results for the linear optical response and the SC. Excitonic effects strongly redistribute the intensity and enhance the SC. From the analysis of the excitonic state in terms of the electronic structure, we explain the difference between the A/B and C excitons in the SC enhancement.

## II. THEORETICAL METHODS

We present the definition of the SC response (Sec. II A) and the real-time approach used to calculate it, as well as the procedures to extract nonlinear conductivity coefficients from the real-time current (Sec. II B). Then, we detail all the computational parameters used in the simulations (Sec. II C). As these are the first calculations of the SC with the Yambo code<sup>26</sup>, in Appendix A we detail the numerical implementation of the current operator. For validation, we compare with existing results on the GeS monolayer<sup>2,4,27–29</sup> (see Supp. Mat.).

### A. The shift current

When a material is irradiated by light, a current is produced. In the perturbative regime, this current can be expressed as an order expansion of the total field strength:

$$J(\omega) = \sigma^{(1)}(\omega)E(\omega) + \sum_{\omega} \sigma^{(2)}(\omega; \omega_1, \omega_2)E(\omega_1)E(\omega_2) + O(E^3), \quad (1)$$

where the summation on  $\omega$  indicates the sum over all distinct  $\omega_1, \omega_2$  pairs. With  $\omega_1, \omega_2 \neq 0$ , the lowest order that produces DC current is the second order when  $\omega = \omega_1 + \omega_2 = 0$ .<sup>30</sup> In case of a monochromatic field,

$$J^{(2)}(\omega = 0) = 2\sigma^{(2)}(0; \omega_1, -\omega_1)E(\omega_1)E(-\omega_1). \quad (2)$$

### B. Equation of motion

We simulate a system under the influence of an external, time-dependent electric field by solving an effective Schrödinger equation.

$$i\hbar \frac{d}{dt} |v_{\mathbf{k},m}\rangle = \left( \hat{H}_{\mathbf{k}}^0 + i\mathcal{E} \cdot \partial_{\mathbf{k}} \right) |v_{\mathbf{k},m}(t)\rangle. \quad (3)$$

where  $|v_{\mathbf{k},m}(t)\rangle$  are the time-dependent valence states and the dipole operator has been replaced with  $\mathbf{r} = i\partial_{\mathbf{k}}$  and the  $\mathbf{k}$ -derivative has been performed using a covariant approach.<sup>31,32</sup> In the following we will omit the time-dependence of  $|v_{\mathbf{k},m}(t)\rangle$  in order to simplify the notation. From the real-time dynamics of the valence states we calculate the current as:

$$J = \frac{f}{(2\pi)^3} \sum_{n=1}^M \langle v_{\mathbf{k}n} | \hat{H}_{\mathbf{k}} \partial_{\mathbf{k}} | v_{\mathbf{k}n} \rangle + c.c. \quad (4)$$

The derivative in  $\mathbf{k}$  space is evaluated by means of finite-difference covariant formulation (see Souza et al. in Ref. 31):

$$\begin{aligned} \tilde{\partial}_{\mathbf{k}} |v_{\mathbf{k}n}\rangle &\simeq \frac{4}{3} \frac{|\tilde{v}_{\mathbf{k}+\Delta\mathbf{k},n}\rangle - |\tilde{v}_{\mathbf{k}-\Delta\mathbf{k},n}\rangle}{2\Delta\mathbf{k}} \\ &\quad - \frac{1}{3} \frac{|\tilde{v}_{\mathbf{k}+2\Delta\mathbf{k},n}\rangle - |\tilde{v}_{\mathbf{k}-2\Delta\mathbf{k},n}\rangle}{4\Delta\mathbf{k}} + O(\Delta\mathbf{k})^4, \quad (5) \end{aligned}$$

where the tilde indicates that we used the covariant derivative in order to deal with the arbitrary phase factor associated with wave functions at different  $\mathbf{k}$ -points.<sup>31,32</sup> In Appendix A, we describe the numerical implementation of Eqs. (4) and (5) in the Yambo code<sup>26</sup>.

In Eq (3), the effective Hamiltonian is chosen depending on the level of accuracy we aim at, from independent-particle approximation (IPA) to the time-dependent adiabatic GW (TD-aGW).<sup>33</sup> The latter approximation is equivalent to the GW+BSE method in the linear response limit.<sup>11,33</sup>

To obtain the second order conductivity corresponding to the SC, we perturb the system with a sinusoidal electric field  $E(t) = E_0\theta(t-t_0)\sin(\omega_0 t)$ , where  $E_0, \omega_0$  are the strength and frequency of the applied electric field and  $\theta$  the Heaviside step function. Further, we add a term to the Hamiltonian to dephase the eigenmodes that are excited upon the field switch-on at  $t_0$ .<sup>32</sup> After transient effects from the field switch-on have decayed, the final current can be written as a Fourier series expansion:  $J(t) = \sum_{j=-N}^N c_j e^{ij\omega_0 t}$ . The coefficients  $c_j$  can be obtained by a discrete Fourier transform by sampling  $J(t)$  on a period  $2\pi/\omega_0$ . The components of the  $n$ -order conductivity tensor are directly related to the  $c_j$  coefficients through powers of the applied electric field. This procedure is the analogue of that used to extract the nonlinear susceptibilities from the polarization density that has been detailed in Refs. 14 and 32. In this case, we extract the conductivity corresponding to the SC from  $c_0 = 2\sigma^{(2)}(0; \omega_0, -\omega_0)E_0^2 + O(E_0^4)$ .

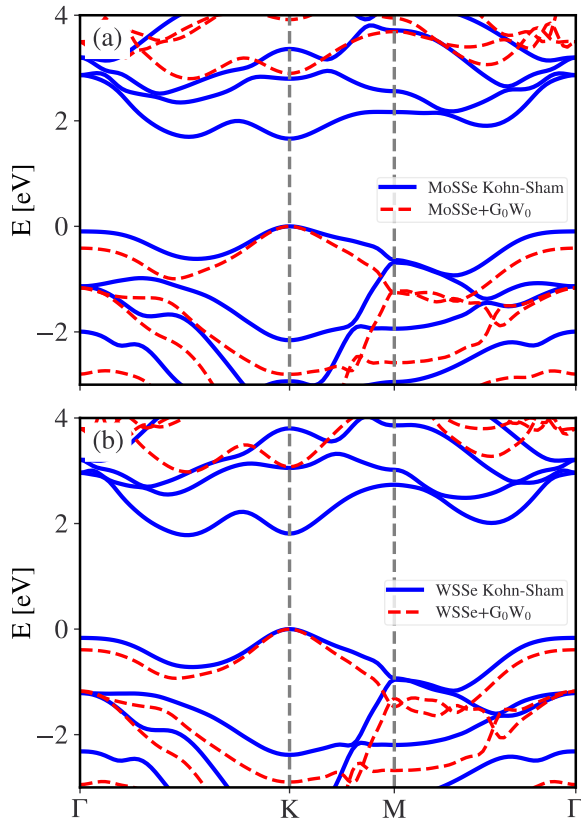


FIG. 1. The electronic band structures of (a) MoSSe and (b) WSSe monolayers, at the Kohn-Sham level (blue solid lines) and including the quasiparticle corrections from  $G_0W_0$  calculations (red dashed lines).

### C. Computational details

The ground states of all the systems studied in this manuscript were calculated using Density Functional Theory (DFT) with the PBE functionals and the DOJO stringent pseudo-potential v4.1 to replace the core electrons.<sup>34</sup> We include also a van der Waals correction to the DFT functional.<sup>35</sup> All DFT calculations were performed with the Quantum ESPRESSO code.<sup>36</sup> The linear and nonlinear optical response and quasiparticle corrections were calculated using the Yambo code<sup>26</sup>. For the quasiparticle correction, the  $G_0W_0$  approximation<sup>10</sup> was applied, where the screened interaction was treated with the Godby-Needs plasmon-pole model (PPM).<sup>37</sup>

We calculated the optical absorption at the independent particle approximation (IPA) on top of Kohn-Sham band structure, adding  $G_0W_0$  corrections (IPA-GW) and including the local-field effects and electron-hole interaction by solving the Bethe-Salpeter equation in the Tamm-Dancoff<sup>11</sup> (GW+BSE). While the IPA and IPA-GW are solved within the linear response framework, the

System	$\mathbf{k}$ -points	$N_b$	$\epsilon_{\text{cut}}$ (Ha)	$\epsilon_{\text{bands}}$	$L_z$ (Å)	$d_{\text{eff}}$ (Å)
MoSSe	$24 \times 24$	19-26	5	400	36.30	6.15
WSSe	$24 \times 24$	19-26	5	400	36.30	3.35

TABLE I. The parameters used in the nonlinear response calculations for MoSSe and WSSe monolayers are:  $\mathbf{k}$ -point sampling; the range of bands for the response functions; the cut-off,  $\epsilon_{\text{cut}}$ , and the number of bands,  $\epsilon_{\text{bands}}$  used to converge the dielectric function  $\epsilon_{\mathbf{G},\mathbf{G}'}$ , and expansion of the Green's function in the GW calculations; the height of the supercell,  $L_z$  and the effective layer thickness,  $d_{\text{eff}}$ .

GW+BSE is formulated as an eigenvalue problem for the two-particle Hamiltonian:

$$\begin{aligned}
 H_{v'c'\mathbf{k}'}^{vck} &= (E_{c\mathbf{k}} - E_{v\mathbf{k}}) \delta_{vv'} \delta_{cc'} \delta_{\mathbf{k}\mathbf{k}'} + \\
 &+ (f_{c\mathbf{k}} - f_{v\mathbf{k}}) \left( 2\bar{V}_{v'c'\mathbf{k}'}^{vck} - W_{v'c'\mathbf{k}'}^{vck} \right)
 \end{aligned} \quad (6)$$

where  $E_{n\mathbf{k}}$  are quasiparticle energies and  $f_{n\mathbf{k}}$  the electronic occupations and  $n$  run over the valence ( $v$ ) and conduction bands ( $c$ ).  $\bar{V}$  is the Coulomb potential derived from the variation of the Hartree term and  $W$  the screened electron-hole interaction derived from the screened exchange.<sup>11</sup> The eigenvectors  $A_{cv\mathbf{k}}^\lambda$  and eigenvalues  $E_\lambda$  of the Hamiltonian in Eq. 6 are respectively the excitonic wave-functions and energies. These quantities are used to build up the macroscopic dielectric function  $\epsilon_M$  which writes:

$$\epsilon_M(\omega) = 1 - 4\pi \sum_{\lambda} \frac{|T_\lambda|^2}{\omega - E_\lambda + i\eta}, \quad (7)$$

where  $T_\lambda = \sum_{cv\mathbf{k}} d_{cv\mathbf{k}} A_{cv\mathbf{k}}^\lambda$  are the excitonic dipoles,  $d_{cv\mathbf{k}}$  are the dipole matrix elements between the Kohn-Sham states with  $d_{cv\mathbf{k}} = \langle v\mathbf{k} | \hat{r} | c\mathbf{k} \rangle$ , and  $i\eta$  with  $\eta$  chosen to be 0.1 eV is a small broadening factor to simulate the experimental spectra. In order to consider isolated monolayers, a cutoff was applied to the Coulomb potential to avoid interaction between periodic replicas along the  $z$ -direction (Rozzi et al. 38).

The nonlinear response is evaluated from the solution of the equation of motions as in Sec. II B at the corresponding levels of theory as for the optical absorption<sup>33</sup>: TD-IP, TD-IP@GW, and TD-aGW. The equations of motion have been solved using the Crank-Nicolson solver<sup>32</sup>, with an integration time of 83 fs and a time-step of 0.01 fs and a dephasing time corresponding to a 0.1 eV spectral broadening. The nonlinear response was extracted from the real-time current using the YamboPy code<sup>39</sup>. All other relevant computational details are presented in Table I. The spin-orbit coupling was not included in the calculations, as it has been shown to have little effect on the nonlinear response of Janus TMDs<sup>21</sup>.

### III. RESULTS

#### A. Atomic and electronic structure

For both MoSSe and WSSe we optimize atomic positions and unit cell at zero pressure by minimizing the enthalpy as implemented in the Quantum Espresso code.<sup>36</sup> We obtained lattice parameters of 6.089 a.u. and 6.090 a.u. respectively for MoSSe and WSSe. Starting from the optimized atomic structure we calculate the electronic bands and then the linear and nonlinear response functions. The electronic band structures are evaluated at the Kohn-Sham (KS) and  $G_0W_0$  levels for both MoSSe and WSSe, results are shown in Fig. 1. For MoSSe, we found a gap of 1.66 eV at the PBE level and 2.80 eV in the  $G_0W_0$  approximation. For WSSe, the KS gap is 1.78 eV while the  $G_0W_0$  corrections increase it to 2.98 eV. These results are in agreement with previous calculations.<sup>40–42</sup> Interestingly, there is a strong  $k$ -dependence of the  $G_0W_0$  corrections for the valence bands. Note that the band gaps in these materials are highly sensitive to calculation details and strain, as shown in Ref. 43, and small differences between computational approaches can cause a transition from direct to an indirect semiconductor in the monolayers. The direct/indirect transition affects light-emission properties, but do not impact significantly light absorption or the SC, which only involves direct electron-hole transitions. Figure 2 shows the band structure of WSSe including information on the atomic orbital nature of the electronic wave functions. Of particular interest are the bands closest to the Fermi energy, as are those contributing to the main features in the shift current response. The states in the top valence and bottom conduction bands are mostly localised on the chalcogen atoms (panel a and b), with the exception for states located close to the minima along the  $MF$  direction which are mostly localised on the W atom. On the top valence band, states at and around  $\Gamma$  are mostly localised on the Se atoms while those around K are mostly localised on the S atoms. The bottom conduction band has mostly an S atom character except around the  $\Gamma$  point. From the corresponding analysis of the band structure in terms of the atomic orbital nature of the electronic wave functions for MoSSe (Supplemental material), we conclude that the localization of the closest states to the Fermi energy is substantially the same as in WSSe.

#### B. Linear and nonlinear response in MoSSe and WSSe

For the two systems, we first present the linear optical absorption, which later serves as a guide for interpreting the SC conductivity. In the bottom panels of Figs. 4 and 5 we report the optical absorbance at different levels of approximation: independent particle (IPA), independent particle on top of the GW band structure

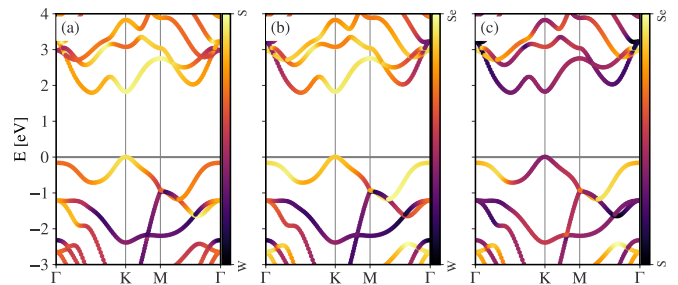


FIG. 2. Projected band structure of WSSe on atomic orbitals. Panel (a): projection weight onto S and W; panel (b): projection weight onto Se and W; panel (c): projection weight onto S and Se.

(IPA-GW), and the GW+BSE approximation.

In Figs. 4 and 5 we can distinguish different excitonic peaks for both MoSSe and WSSe: in particular the A/B peak around 2 eV and the C peaks around the 3 eV. Notice that as we did not include spin-orbit coupling, the ground state exciton (A) and the spin-orbit split exciton (B) are degenerate. The strongest feature in both spectra are the C-excitons, which we found corresponds to the strongest enhancement of the SC. For this reason we analyze them in detail.

We consider the two most intense excitations,  $C_1$  at 3.02 eV and  $C_2$  at 3.19 eV for WSSe, together with the A/B exciton at 2.33 eV, indicated with vertical lines in Fig. 5. We then projected their exciton weights on  $k$ -points in the full Brillouin zone  $W_{\mathbf{k}}^{\lambda} = \sum_{cv} |A_{cv\mathbf{k}}^{\lambda}|^2$ , top panel of Fig. 3, and on the valence/conduction bands along the band structure of WSSe,  $W_{c/v,\mathbf{k}}^{\lambda} = \sum_{v/c} |A_{cv\mathbf{k}}^{\lambda}|^2$ , bottom panel of Fig. 3. The A/B exciton originated from electron-hole transitions around K, the  $C_1$  exciton originated from electron-hole transitions along K- $\Gamma$ , the  $C_2$  exciton from electron-hole transitions around  $\Gamma$ . For all three excitons, the holes are in the top valence band and the electrons in the bottom conduction band. By comparing the distribution of the  $W_{c/v,\mathbf{k}}^{\lambda}$  with the atomic orbital projected band structures, (Supplemental Material), we can deduce the spatial localization of the electron-hole pairs contributing to each exciton. For the A/B exciton, both electrons and holes are mostly localized on the chalcogen atoms. Being the composition of the bottom conduction and top valence around K very similar, we deduce the electron and hole are localized around the same atom. For the  $C_1$  exciton, while the electrons are mostly localized around the S atoms, the hole are partially localized on the Se atoms as well. For the  $C_2$  exciton, holes are more localised on the tungsten and electrons more on the S atoms.

A similar analysis holds for the C-excitons around 3 eV of MoSSe (see Supplemental Material). Note that, for MoSSe, the most intense features are at higher energies than the C excitons. Nevertheless, as these features are out of visible range and so not relevant for photovoltaic

applications, we do not provide an analysis of these excited states.

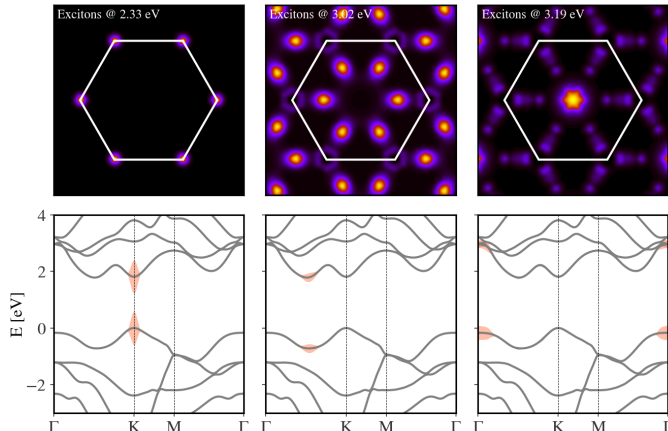


FIG. 3. Exciton analysis in WSSe. Top left (right) panel: the projection onto the BZ of the A/B,  $C_1$  and  $C_2$  excitons. Bottom left (right) panel: the projection along the WSSe band structure of the A/B,  $C_1$  and  $C_2$  excitons.

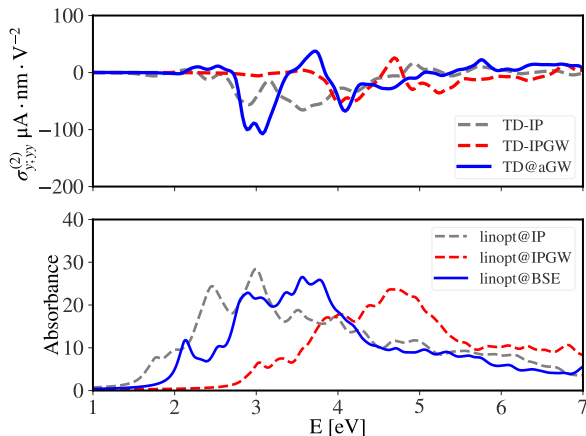


FIG. 4. Shift current along the  $yyy$  direction for MoSSe (upper panel) compared with the linear absorption (lower panel), at the IP (gray dashed lines), IPGW (red dashed lines) and GW+BSE (blue solid lines) levels.

Next we consider the SC. Figures 5 and 4 show the SC of MoSSe and WSSe at the three levels of approximation.: In the nonlinear response function, the gap widening induced by GW corrections substantially modifies the spectral intensity by suppressing the SC conductivity. Including excitonic effects redshifts the full spectrum and restores its intensity, albeit with a significant redistribution with respect to the TD-IP. In both systems, the SC conductivity is strongly suppressed in correspondence of the A/B exciton, while it is strongly enhanced in correspondence of the C-excitons. A similar intensity redistribution has been observed in other

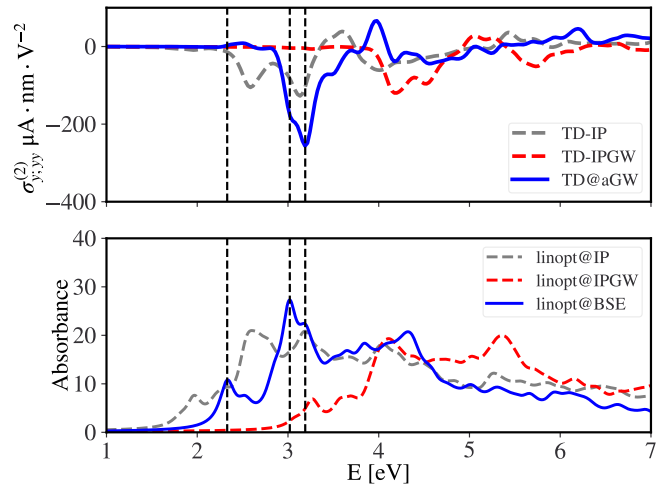


FIG. 5. Shift current along the  $yyy$  direction in WSSe (upper panel) compared with the linear absorption (lower panel), at the IP (gray dashed lines), IPGW (red dashed lines) and GW+BSE (blue solid lines) levels.

2D dichalcogenides in second-harmonic generation<sup>44</sup> and sum-frequency generation.<sup>14</sup> The relation between SHG and SC is also discussed in the work of Morimoto and Nagaosa in Ref. 5.

To explain the stark difference of the SC at resonance with the A/B and C excitons, we refer to the analysis in terms of electron-hole pairs. While for the A/B exciton the holes and electrons are localized around the same atom, for the C excitons the electron and holes are localized on different sites. We thus argue that following a photo-excitation at resonance with the C excitons there is a shift of the center of electronic charge, which is the physical origin of the SC. We now highlight the key differences between the two systems, MoSSe and WSSe. Two important differences stand out as we move from one to the other: the first is the different band gaps, reflected in the shift of the SC spectra. The WSSe spectra starts at slightly higher energies than that of MoSSe. Second, in WSSe, C-excitons are more intense and better separated from higher excitons than in MoSSe. These differences will be important for selecting the best material having a response in the desired energy range in experimental devices. Finally, we found that the SC response of Janus dichalcogenides at resonance, renormalized with the effective thickness, has an intensity comparable to that of the strongest known 2D materials in the scientific literature<sup>2</sup>, making 2D-Janus an interesting building block for future devices.

#### IV. CONCLUSIONS

We studied the SC response of two-dimensional (2D) Janus dichalcogenides, MoSSe and WSSe, using a real-time approach that included correlation effects in the

electronic band structures and response functions. We found that, in both systems, excitonic effects strongly enhance the SC conductivity at resonance with C-excitons, while suppresses it at resonance with the A/B exciton. As the SC originates from the shift of the center of electron charge following photo-excitations, we rationalize this result by noting that in the A/B exciton, the electrons and holes are localized around the same atomic site—thus no shift of the center of electron charge—while in the C excitons, the real-space distribution of electrons and holes differs significantly, so following a photoexcitation resonant with the C excitons, there is a shift of the center of electron charge and thus a photocurrent. To transform these materials into devices and take advantage of their significant response, the  $C_{3V}$  symmetry must be broken. This can be achieved by combining the materials into heterostructures with tensile strain<sup>23</sup>, or by creating nanotubes along the non-zero response direction<sup>45</sup>. Furthermore, the possibility of inverting the SC direction by inverting the z-axis of Janus dichalcogenides and using their internal electric field to interact with closest layers endows these materials with extra tunability.

## ACKNOWLEDGMENTS

C.A. and Y.M. acknowledge B. Demoulin and A. Saul for the management of the computer cluster *Rosa*. C.A. and Y.M. acknowledge ANR project COLIBRI No. ANR-22-CE30-0027. C.A. acknowledges funding from European Research Council MSCA-ITN TIMES under grant agreement 101118915. M.G. acknowledges funding from the UKRI Horizon Europe Guarantee funding scheme (EP/Y032659/1). C.A. acknowledge Davide Sangalli for helping developing the Yambo code.

### Appendix A: Numerical evaluation of the current operator

In Eq. (4) the current operator is written in term of a covariant  $k$ -derivative of the periodic part of the time-dependent valence bands. This derivative is numerically evaluated on a finite  $k$ -point grid as shown in Eq. (5). In this Appendix, we show how the formula for current is implemented in the Yambo code<sup>26</sup>. All operators and wave-functions that appear in the equations of motions are expanded in the Kohn-Sham (KS) basis set  $|u_{\mathbf{k},n}\rangle$ . In this basis, the periodic part of the time-dependent valence bands  $|v_{\mathbf{k},n}\rangle$  and their covariant counterpart  $|\tilde{v}_{\mathbf{k}i\sigma,n}\rangle$

reads:

$$|v_{\mathbf{k},n}(t)\rangle = \sum_{j=1}^{\infty} c_{\mathbf{k},n,j}(t) |u_{\mathbf{k},j}\rangle$$

$$|\tilde{v}_{\mathbf{k}i\sigma,n}\rangle = \sum_{m=1}^M (\tilde{S}_{\mathbf{k}i\sigma}^{-1})_{m,n} |v_{\mathbf{k}i\sigma,m}\rangle$$

where  $M$  is the number of valence bands, and  $\tilde{S}_{\mathbf{k},i\sigma}$  is the overlap matrix between real-time valence states. The indices  $m, n$  run on the valence bands.  $\{\mathbf{k}i\sigma\} = \mathbf{k} + \sigma\Delta\mathbf{k}_i$  with  $\sigma = \pm 1$  and  $i$  labeling the displacement along the reciprocal lattice vectors in the  $\mathbf{k}$ -grid. The overlap matrix  $S_{\mathbf{k},i\sigma}$  between time-dependent valence states reads:

$$\left[ \tilde{S}_{\mathbf{k}i\sigma} \right]_{m,n} = \langle v_{\mathbf{k},m}(t) | v_{\mathbf{k}i\sigma,n}(t) \rangle \quad (\text{A1})$$

$$\left[ \tilde{S}_{\mathbf{k}i\sigma} \right]_{m,n} = \sum_{j,l} c_{\mathbf{k},m,j}^*(t) c_{\mathbf{k}i\sigma,n,l}(t) (S_{\mathbf{k}i\sigma})_{j,l} \quad (\text{A2})$$

$$[S_{\mathbf{k}i\sigma}]_{j,l} = \langle u_{\mathbf{k},j} | u_{\mathbf{k}i\sigma,l} \rangle \quad (\text{A3})$$

We apply  $\hat{H}_{\mathbf{k}}^0$  to the bra and get:

$$\langle v_{\mathbf{k}n} | \hat{H}_{\mathbf{k}}^0 = \sum_{j=1}^{\infty} c_{\mathbf{k},n,j}^*(t) \epsilon_{\mathbf{k},j} \langle u_{\mathbf{k},j} | \quad (\text{A4})$$

$$= \sum_{j=1}^{\infty} \tilde{c}_{\mathbf{k},n,j}^*(t) \langle u_{\mathbf{k},j} |$$

where

$$\tilde{c}_{\mathbf{k},n,j}^* = c_{\mathbf{k},n,j}^* \epsilon_{\mathbf{k},j}. \quad (\text{A5})$$

Finally, we express also  $|\tilde{v}_{\mathbf{k}i\sigma,n}\rangle$  in the KS basis set as:

$$|\tilde{v}_{\mathbf{k}i\sigma,n}\rangle = \sum_{m=1}^M (\tilde{S}_{\mathbf{k}i\sigma}^{-1})_{m,n} |v_{\mathbf{k}i\sigma,m}\rangle$$

$$= \sum_{m=1}^M (\tilde{S}_{\mathbf{k}i\sigma}^{-1})_{m,n} \sum_{j=1}^{\infty} c_{\mathbf{k}i\sigma,m,j}(t) |u_{\mathbf{k}i\sigma,j}\rangle$$

$$= \sum_{m=1}^M (\tilde{S}_{\mathbf{k}i\sigma}^{-1})_{m,n} \sum_{j,l=1}^{\infty} c_{\mathbf{k}i\sigma,m,j}(t) [S_{\mathbf{k},i\sigma}^*]_{j,l} |u_{\mathbf{k},l}\rangle$$

$$= \sum_{l=1}^{\infty} \tilde{c}_{\mathbf{k}i\sigma,n,l} |u_{\mathbf{k},l}\rangle$$

where

$$\tilde{c}_{\mathbf{k}i\sigma,n,l}(t) = \sum_{m=1}^M (\tilde{S}_{\mathbf{k},i\sigma}^{-1})_{m,n} \sum_{j=1}^{\infty} c_{\mathbf{k}i\sigma,m,j}(t). \quad (\text{A6})$$

Using the definition of  $\tilde{c}$  [Eq. (A6)] and  $\bar{c}$  [Eq. (A5)], we can write the bra-ket that appears in the current, Eq. 5, as:

$$\langle v_{\mathbf{k}n} | \hat{H}_{\mathbf{k}}^0 | \tilde{v}_{\mathbf{k}i\sigma,n} \rangle = \sum_{j=1}^{\infty} \tilde{c}_{\mathbf{k},n,j}^*(t) \tilde{c}_{\mathbf{k}i\sigma,n,j}(t) \quad (\text{A7})$$

Using Eq. (A7) we can rewrite all Eq. (5) in the KS basis.

- <sup>1</sup> A. M. Cook, B. M. Fregoso, F. De Juan, S. Coh, and J. E. Moore, *Nature communications* **8**, 14176 (2017).
- <sup>2</sup> Y.-H. Chan, D. Y. Qiu, F. H. da Jornada, and S. G. Louie, *Proceedings of the National Academy of Sciences* **118**, e1906938118 (2021).
- <sup>3</sup> F. Hipolito, T. G. Pedersen, and V. M. Pereira, *Physical Review B* **94**, 045434 (2016).
- <sup>4</sup> J. Esteve-Paredes, M. García-Blázquez, A. Uría-Álvarez, M. Camarasa-Gómez, and J. Palacios, *npj Computational Materials* **11**, 13 (2025).
- <sup>5</sup> T. Morimoto and N. Nagaosa, *Phys. Rev. B* **94**, 035117 (2016).
- <sup>6</sup> R. Fei, L. Z. Tan, and A. M. Rappe, *Physical Review B* **101**, 045104 (2020).
- <sup>7</sup> Y. Zhang, T. Ideue, M. Onga, F. Qin, R. Suzuki, A. Zak, R. Tenne, J. Smet, and Y. Iwasa, *Nature* **570**, 349 (2019).
- <sup>8</sup> J. Krishna, P. Garcia-Goiricelaya, F. de Juan, and J. Ibañez Azpiroz, *Phys. Rev. B* **108**, 165418 (2023).
- <sup>9</sup> B. Kim, N. Park, and J. Kim, *Nature Communications* **13**, 3237 (2022).
- <sup>10</sup> F. Aryasetiawan and O. Gunnarsson, *Rep. Prog. Phys.* **61**, 237 (1998).
- <sup>11</sup> G. Strinati, *Riv. Nuovo Cimento* **11**, 1 (1988).
- <sup>12</sup> S. Grillo, E. Cannuccia, M. Palummo, O. Pulci, and C. Attaccalite, *SciPost Physics Core* **7**, 081 (2024).
- <sup>13</sup> C. Attaccalite, M. Grüning, H. Amara, S. Latil, and F. Ducastelle, *Physical Review B* **98**, 165126 (2018).
- <sup>14</sup> M. N. Pionteck, M. Grüning, S. Sanna, and C. Attaccalite, *arXiv preprint arXiv:2503.07095* (2025).
- <sup>15</sup> A.-Y. Lu, H. Zhu, J. Xiao, C.-P. Chuu, Y. Han, M.-H. Chiu, C.-C. Cheng, C.-W. Yang, K.-H. Wei, Y. Yang, *et al.*, *Nature nanotechnology* **12**, 744 (2017).
- <sup>16</sup> J. Zhang, S. Jia, I. Kholmanov, L. Dong, D. Er, W. Chen, H. Guo, Z. Jin, V. B. Shenoy, L. Shi, and J. Lou, *ACS Nano* **11**, 8192 (2017).
- <sup>17</sup> Y.-C. Lin, C. Liu, Y. Yu, E. Zarkadoula, M. Yoon, A. A. Puztzky, L. Liang, X. Kong, Y. Gu, A. Strasser, H. M. I. Meyer, M. Lorenz, M. F. Chisholm, I. N. Ivanov, C. M. Rouleau, G. Duscher, K. Xiao, and D. B. Geohegan, *ACS Nano* **14**, 3896 (2020).
- <sup>18</sup> E. Torun, F. Paleari, M. V. Milosević, L. Wirtz, and C. Sevik, *Nano Letters* **23**, 3159 (2023), pMID: 37037187.
- <sup>19</sup> C. Xia, W. Xiong, J. Du, T. Wang, Y. Peng, and J. Li, *Phys. Rev. B* **98**, 165424 (2018).
- <sup>20</sup> B. D. Aparicio-Huacarpuma, M. L. Pereira Júnior, A. M. A. Silva, A. C. Dias, and L. A. Ribeiro Júnior, *ACS Applied Energy Materials* **8**, 6634 (2025).
- <sup>21</sup> A. Strasser, H. Wang, and X. Qian, *Nano Letters* **22**, 4145 (2022).
- <sup>22</sup> M. Chen, S.-B. Yu, D. Zhang, and J. Li, *Chin. Phys. Lett.* **40** (2023), 10.1088/0256-307X/40/8/087201.
- <sup>23</sup> N. T. Hung, K. Zhang, V. Van Thanh, Y. Guo, A. A. Puztzky, D. B. Geohegan, J. Kong, S. Huang, and R. Saito, *ACS nano* **17**, 19877 (2023).
- <sup>24</sup> C. Yang, Q. Lin, Y. Sato, Y. Gao, Y. Zheng, T. Wang, Y. Ma, W. Dai, W. Li, M. Maruyama, *et al.*, *Small*, 2412454 (2025).
- <sup>25</sup> This component is equal, minus a sign, to the other non-zero in-plane components.
- <sup>26</sup> D. Sangalli, A. Ferretti, H. Miranda, C. Attaccalite, I. Marri, E. Cannuccia, P. Melo, M. Marsili, F. Paleari, A. Marrazzo, G. Prandini, P. Bonfà, M. O. Atambo, F. Affinito, M. Palummo, A. Molina-Sánchez, C. Hogan, M. Gruning, D. Varsano, and A. Marini, *Journal of Physics: Condensed Matter* **31**, 325902 (2019), <https://www.yambo-code.eu/>.
- <sup>27</sup> J. Ibañez Azpiroz, S. S. Tsirkin, and I. Souza, *Phys. Rev. B* **97**, 245143 (2018).
- <sup>28</sup> L. C. Gomes, P. E. Trevisanutto, A. Carvalho, A. S. Rodin, and A. H. Castro Neto, *Phys. Rev. B* **94**, 155428 (2016).
- <sup>29</sup> B. Cunningham, M. Grüning, P. Azarhoosh, D. Pashov, and M. van Schilfgaarde, *Phys. Rev. Mater.* **2**, 034603 (2018).
- <sup>30</sup> J. E. Sipe and A. I. Shkrebtii, *Phys. Rev. B* **61**, 5337 (2000).
- <sup>31</sup> I. Souza, J. Íñiguez, and D. Vanderbilt, *Physical Review B* **69**, 085106 (2004).
- <sup>32</sup> C. Attaccalite and M. Grüning, *Physical Review B* **88**, 235113 (2013).
- <sup>33</sup> C. Attaccalite, M. Grüning, and A. Marini, *Phys. Rev. B* **84**, 245110 (2011).
- <sup>34</sup> M. van Setten, M. Giantomassi, E. Bousquet, M. Verstraete, D. Hamann, X. Gonze, and G.-M. Rignanese, *Computer Physics Communications* **226**, 39 (2018), <http://www.pseudo-dojo.org/>.
- <sup>35</sup> S. Grimme, *Journal of computational chemistry* **27**, 1787 (2006).
- <sup>36</sup> P. Giannozzi *et al.*, *J. Phys. Condens. Matter* **21**, 395502 (2009), <http://www.quantum-espresso.org>.
- <sup>37</sup> M. Stankovski, G. Antonius, D. Waroquiers, A. Miglio, H. Dixit, K. Sankaran, M. Giantomassi, X. Gonze, M. Côté, and G.-M. Rignanese, *Phys. Rev. B* **84**, 241201 (2011).
- <sup>38</sup> C. A. Rozzi, D. Varsano, A. Marini, E. K. Gross, and A. Rubio, *Phys. Rev. B* **73**, 205119 (2006).
- <sup>39</sup> F. Paleari, A. Molina-Sánchez, M. Nalabothula, R. Reho, M. Bonacci, J. M. Castelo, J. Cervantes-Villanueva, M. Pionteck, M. Silveti, C. Attaccalite, and H. Pereira Coutada Miranda, “YamboPy,” (2025).
- <sup>40</sup> C. Long, Y. Dai, and H. Jin, *Phys. Rev. B* **104**, 125306 (2021).
- <sup>41</sup> F. Li, W. Wei, B. Huang, and Y. Dai, *The Journal of Physical Chemistry C* **124**, 1667 (2019).
- <sup>42</sup> F. Li, Y. Wang, Y. Liang, Y. Dai, B. Huang, and W. Wei, *Journal of Physics: Condensed Matter* **35**, 304005 (2023).
- <sup>43</sup> B. Hou, Y. Zhang, H. Zhang, H. Shao, C. Ma, X. Zhang, Y. Chen, K. Xu, G. Ni, and H. Zhu, *The journal of physical chemistry letters* **11**, 3116 (2020).
- <sup>44</sup> J. Ruan, Y.-H. Chan, and S. G. Louie, *Nano Lett.* **24**, 15533 (2024).
- <sup>45</sup> C. Yang, Q. Lin, Y. Sato, Y. Gao, Y. Zheng, T. Wang, Y. Ma, W. Dai, W. Li, M. Maruyama, *et al.*, *Small*, 2412454 (2025).